Nanocomposites of transition-metal carbides on reduced graphite oxide as catalysts for the hydrogen evolution reaction

Seok Ki Kim[a], Yang Qiu[a], Yin-Jia Zhang[b], Robert Hurt[a], Andrew Peterson[a],[*]

[a] School of Engineering, Brown University, Providence, RI 02912, United States
[b] Department of Chemistry, Brown University, Providence, RI 02912, United States

ABSTRACT

Transition metal carbides (TMC), Mo_2C, Fe_3C, and $WC\cdot W_2C$, were synthesized as well-dispersed nanoparticles on a reduced graphite oxide (rGO) substrate and each of their hydrogen evolution reaction (HER) activities was compared with that of a bulk TMC powder. Among the TMC/rGO nanocomposites, only Mo_2C/rGO exhibited an obvious increase in the capacitance-normalized current density compared to the bulk powder. We performed density functional theory calculations which suggest that the distinctive activity of Mo_2C can be attributed to the structure-sensitive binding energies of atomic H, which binds less strongly on the stepped surface than the flat surface of Mo_2C, while other TMCs do not exhibit clear structure-sensitivity. The charge transfer resistances were significantly reduced by using rGO as the substrate, but its correlation with the HER activity was not strong. An analysis of the kinetic data suggested that hydrogen evolution on the TMC surface follows the Volmer–Tafel mechanism with the Tafel step (recombination) rate limiting, which is responsible to the weak correlation between the charge transfer properties and HER activity.

1. Introduction

When driven by renewable resources such as wind, solar, or nuclear energy, electrocatalytic water splitting is one of the most promising technologies for carbon-free H_2 production [1–3]. The H_2 evolution reaction (HER) catalyst, located at the cathode of the electrolysis device, has a major influence on the efficiency and durability of the system. To date, Pt or Pt-based alloy materials have been reported to exhibit the highest catalytic activities for the HER in acidic media [4], but their scarcity and resulting high cost hinder large-scale applications [5].

When new catalyst materials are developed for the HER, certain design principles are taken into account. Thermodynamically, an ideal catalyst should exhibit a free energy of adsorbed atomic hydrogen that places it close to the equilibrium with the free energy of gaseous H_2: too weak or too strong hydrogen binding will induce an elementary step that is uphill in free energy along the reaction pathway, decreasing catalytic activity [6–8]. Second, improvements in electrochemical kinetic behaviors, through an increased electron conductivity that facilitates the charge transfer kinetics at the solid-liquid interface are often pursued [9,10].

Among the promising approaches to develop an efficient catalyst that consists of earth-abundant (and therefore cost-effective) materials,

transition metal carbides (TMC) in a wide variety of structures have shown considerable activity as HER catalysts [11–31]. From a materials-engineering perspective, two recurrent emphases can be found in many of these studies: (1) nanostructuring of TMC, and (2) using carbon allotropes as a substrate of the electrocatalyst. Both can play crucial roles in the catalyst activity, by adjusting the hydrogen binding energy and electron conductivity of catalyst materials, respectively [24–29].

In this work, we offer a comprehensive study dealing with hydrogen binding energy, electron conductivity and their synergistic effect on the HER mechanism among different TMC nanostructures deposited on carbon substrates. The catalytic properties of TMCs largely depend on their composition, surface area, and surface structure which are closely associated with the synthetic method. Here, we make use of a recent demonstration of the controlled synthesis of well-dispersed Mo_2C nanoparticles on reduced graphite oxide (rGO) substrates; these were synthesized at a relatively low temperature (650 °C) using a solvothermal process followed by carbothermal hydrogen reduction [32]. In the present investigation, we demonstrate the above method in the synthesis of three different TMC species, including molybdenum, tungsten and iron carbides, and assess their catalytic activity for the HER using both experimental and theoretical means. The aforementioned thermodynamic and kinetic aspects must be simultaneously considered to describe the activity of the TMC catalysts; thus, with

---
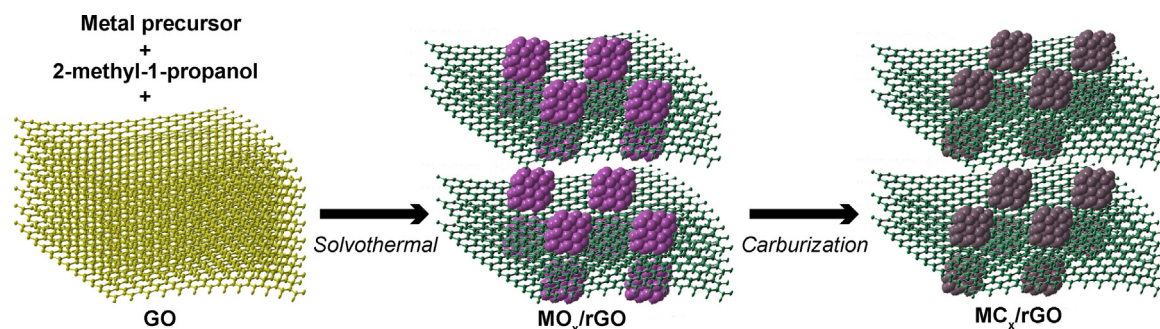
Fig. 1. Schematic illustration of synthetic procedure of TMC/rGO nanocomposite. GO, rGO, TMO denote graphite oxide, reduced graphite oxide, and transition metal oxide, respectively.

regard to the hydrogen binding energy and charge transfer properties, effects of the particle size and rGO substrate were investigated to provide insights into the HER mechanism on these materials.

2. Methods

2.1. Catalyst preparation

Three different TMCs (Fe_3C, Mo_2C, and WC) were synthesized as nanoparticles on reduced graphite oxide (rGO) by a modification of a method we reported previously [32]. A schematic illustration of the synthesis of TMC/rGO nanocomposites is shown in Fig. 1. Graphite oxide (GO) was synthesized by chemical oxidation of graphite powder via the modified Hummer's method [33,34]. In 6 mL of 2-methyl-1-propanol (HPLC grade, Sigma–Aldrich), the metal precursor ($Fe(acac)_3$, $MoO_2(acac)_2$, or $W[OCH(CH_3)_2]_6$, Sigma–Aldrich) was dissolved and 300 mg of GO was dispersed in a ratio to make 25 wt% metal/GO composites. The solution–GO mixture was ultrasonicated for 1 h to obtain a suspension, which was then introduced into a custom-made high pressure cylindrical reactor of 10.6 mL volume (1.3 cm of diameter; 8.0 cm of height). The reactor was made with Type-316 stainless steel with wall thickness of 1.5 cm, allowing it to contain pressures of 35 MPa at 500 °C. After being sealed with a high-pressure coned plug, the reactor was immersed and heated in a sand bath at a temperature of 400 °C for 1 h during which solvothermal precipitation of the metal oxide and reduction of GO were carried out by the supercritical alcohol [32], The estimated pressure inside the reactor was 14.4 MPa at 400 °C, which ensured the supercritical phase of the solvent. (The critical point of 2-methyl-1-propanol is 4.5 MPa and 275 °C.) The mixture was then quenched to room temperature by immersion of the reactor in a water bath. The resultant was then washed and filtered with isopropanol to remove soluble impurities, and dried in a vacuum oven at 60 °C overnight.

Carburization of the rGO-supported metal oxides was conducted in a tube furnace. Since the transformation of each metal oxide into carbide depends to a large extent on its condition [35], we tested various gas compositions, temperatures, and ramping rates to find optimal carburization conditions, which are discussed in detail in Section 3.1.

For comparison, commercial bulk WC powder (average particle size of 2 μm, Sigma–Aldrich), bulk Mo_2C powder (average particle size of 3 μm, Sigma–Aldrich), and Pt/C (5 wt%, Sigma–Aldrich) were used as-purchased. Bulk Fe_3C was synthesized from Fe_2O_3 (average particle size of 3 μm, NOAH Technologies Corp.) using a carbothermal reaction, which was performed by flowing 20% CH_4/H_2 gas mixture at a rate of 100 mL/min with heating at 10 °C/min to 850 °C, holding for 1 h.

2.2. Electrochemical measurement

Hydrogen evolution activities of the catalysts were measured by linear sweep voltammetry (LSV) experiments, which were carried out

with a rotating disk electrode (RDE, Pine Research Instrumentation) in a three electrode cell containing 0.5 M H_2SO_4 saturated with Ar. To fabricate the working electrode, a catalyst ink was prepared by dispersing 20 mg of catalyst powder in a mixture of 2 mL of deionized water and 20 μL of 5% Nafion solution (D520, Ion Power) with ultrasonication for 5 min. 15 μL of the catalyst ink was dropped onto a glassy carbon electrode (0.196 cm^2), which was then dried overnight under atmospheric pressure and temperature. The Ag/AgCl electrode and Pt wire were employed as reference and counter electrodes, respectively. All reported voltages were converted to the reversible hydrogen electrode scale, denoted as V_{RHE}. Prior to the LSV measurement, the working electrode was stabilized by cyclic voltammetry (CV) performed at a scan rate of 10 mV/s in the range of −0.4 to 0.1 V_{RHE}. The current density was stabilized within 10–20 cycles of CV scans; then the LSV experiments were performed at a scan rate of 5 mV/s with a rotation speed of 1000 rpm. We note that Pt dissolution from the counter electrode and its subsequent deposition on the working electrode is not expected to occur in our experimental conditions [36,37]. After the CV stabilization, no significant change in catalyst performance was observed during CV or LSV measurements, as previously reported for similar systems [38].

Potentiostatic electrochemical impedance spectroscopy (PEIS) for the working electrodes was performed in a frequency range from 1 MHz to 50 Hz at −0.4 V_{RHE}. An equivalent-circuit model containing one or two constant-phase element(s) (CPE) was adopted to fit the experimental PEIS spectra so that the charge-transfer resistances, R_{ct}, could be calculated (EC-Lab software, Biologic). The uncompensated resistance, R_u, was also obtained from the PEIS spectra and corrected for each HER experiment. 85% of the R_u was automatically compensated using the potentiostat, which left 15% to be manually corrected as follows [39]

$$E_{100\% \text{ corrected}} = E_{85\% \text{ corrected}} - 0.15iR_u \tag{1}$$

where i is cell current in A. Since the PEIS spectra obtained at the open-circuit potential were not fittable for the porous catalysts used in the present study, electric double layer capacitances (C_{dl}) values, a function of CPE, could not be obtained from this technique. Instead of the PEIS, CV experiments were performed to obtain C_{dl} values. Scan rates were varied at 5, 10, 20, and 50 mV/s in the range of 0–0.5 V_{RHE}. From the CV results, C_{dl} values were calculated by plotting capacitive charging current, i_c, at open-circuit potential against scan rates, dE/dt, as follows [40]

$$i_c = \frac{i_+ - i_-}{2} = C_{dl}\frac{dE}{dt} \tag{2}$$

where i_+ and i_- denote anodic and cathodic capacitive currents, respectively.

2.3. Catalyst characterization

The structure and crystallite size of all (synthesized and purchased) electrocatalysts were analyzed using powder X-ray diffraction (XRD,

Table 1
Lattice parameters calculated in the present study.

Material	Space group	Experimental parameters[a] (Å)	DFT parameters (Å)	Cell angle (°)
Fe_3C	Pnma	$a = 5.08, b = 6.75, c = 4.51$	$a = 4.92, b = 6.68, c = 4.45$	$\alpha = \beta = \gamma = 90$
Mo_2C	Pbcn	$a = 4.75, b = 6.01, c = 5.21$	$a = 4.83, b = 6.15, c = 5.29$	$\alpha = \beta = \gamma = 90$
WC	P6m2	$a = b = 2.90, c = 2.84$	$a = b = 2.93, c = 2.85$	$\alpha = \beta = 90, \gamma = 120$
W_2C	P31m	$a = b = 5.18, c = 4.72$	$a = b = 5.14, c = 4.91$	$\alpha = \beta = 90, \gamma = 120$

[a] Experimental values reported in previous studies [44–46].
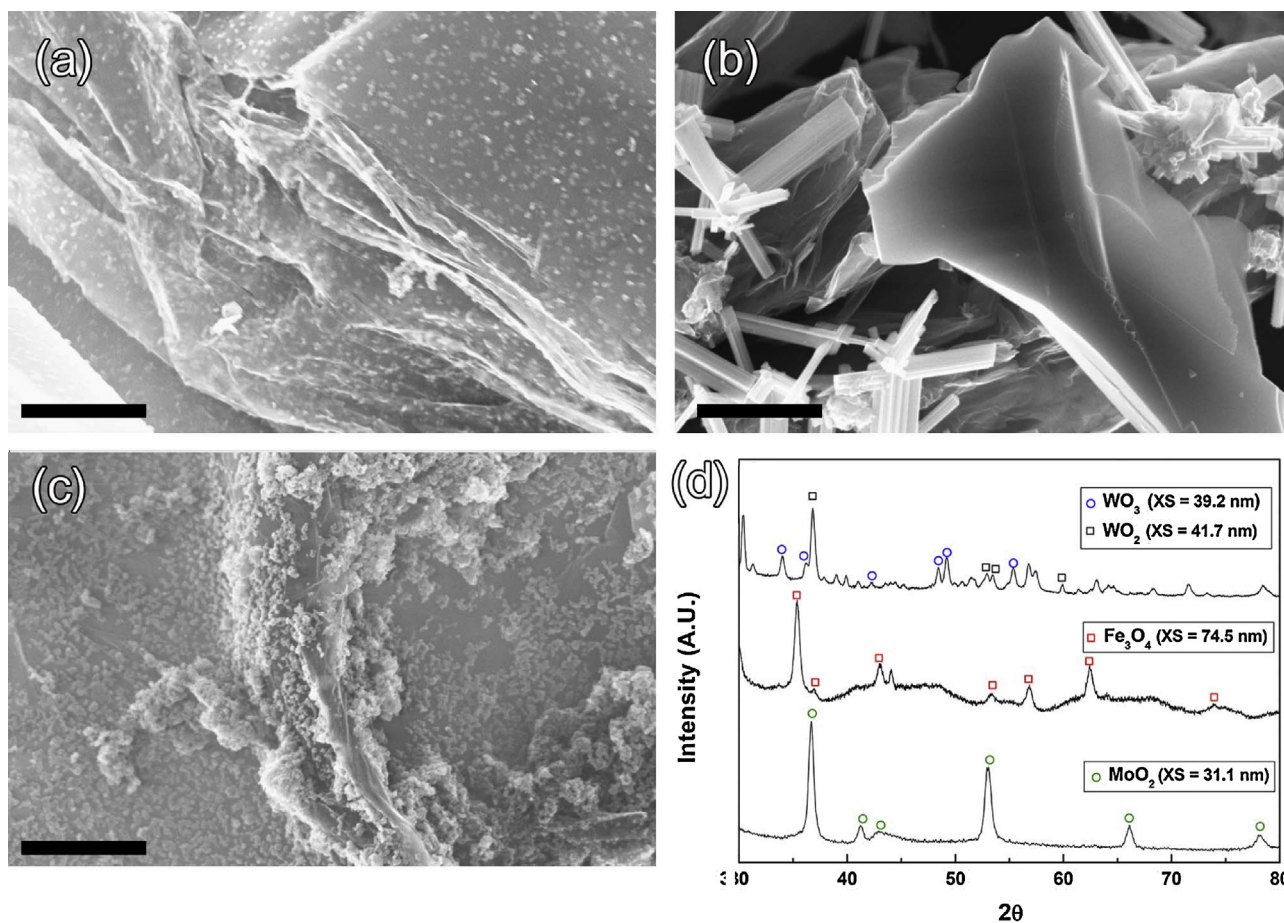
Fig. 2. Scanning electron microscopy (SEM) images of (a) MoO_2/rGO, (b) Fe_3O_4/rGO, and (c) WO_2·WO_3/rGO. The scale indicates 1 μm. (d) shows XRD patterns of rGO-supported metal oxides. XRD peaks were assigned using ICDD card numbers 54-508, 32-1393, 19-629, and 32-671 for WO_3, WO_2, Fe_3O_4, and MoO_2, respectively. Crystallite sizes (XS) calculated based on XRD were also shown.

Bruker D8) equipped with Cu Kα radiation and 2D Vantec 500 detectors. XRD peaks were assigned using the database from the International Centre for Diffraction Data (ICDD). Crystallite sizes were calculated based on the Scherrer formula using the main peak of the crystal domain, that is, 2θ of 55.3°, 36.8°, 35.4°, 36.6°, 52.3°, 48.4°, 44.5°, and 39.4° for WO_3, WO_2, Fe_3O_4, MoO_2, W_2C, WC, Fe_3C, and Mo_2C, respectively. The morphology of the rGO-supported catalysts was observed using scanning electron microscope (SEM, LEO 1530) at a voltage of 20 kV.

2.4. Electronic structure calculations

The binding energy of atomic hydrogen on model catalyst surfaces was calculated via density functional theory (DFT), in the open-source planewave/pseudopotential code DACAPO [41,42]. The exchange–correlation interaction was treated with the revised Perdew--Burke–Ernzerhof (RPBE) functional of Hammer et al. [43] within a generalized gradient approximation (GGA).

The lattice constants of the studied metal carbides were obtained by bulk calculations, which are close to the experimental values [44–46] as shown in Table 1.

To model flat surfaces, the most close-packed surface orientations, $Mo_2C(100)$, $Fe_3C(001)$, WC(0001), and $W_2C(0001)$ were generated as periodically repeated slabs consisting of $2 \times 2 \times 4$ metal atoms ($2 \times 3 \times 4$ for Fe_3C) in the x, y, and z directions, where the bottom two layers were fixed at the bulk geometry and the upper two layers were allowed to fully relax. Stepped surfaces were generated by tilting the flat surfaces on the basis of the z axis, giving $Mo_2C(201)$, $Fe_3C(102)$, WC(10$\bar{1}$2), and $W_2C(10\bar{1}2)$. A vacuum distance of 12 Å was employed for all surface calculations to prevent interaction between slabs separated along the z direction.

The cutoff energies of the planewave and density were set to 340.15 and 500 eV, respectively. Bulk and surface calculations were performed using k-point samplings of ($8 \times 8 \times 8$) and ($4 \times 4 \times 1$) of the Brillouin zone, respectively. The convergence criterion for optimization of atomic geometry was less than 0.05 eV/Å of a maximum force on any

unconstrained atom.

Due to the heterogeneity of surface geometries in carbides, various types of adsorption sites are present, especially on the stepped surfaces. On a given catalyst surface, sites were searched for atomic hydrogen adsorption using constrained minima hopping [47], which is based on the original minima hopping algorithm of Goedecker [48] but employing a Hookean constraint between the hydrogen atom and a surface boundary 2 Å above the surface, preventing volatilization of the hydrogen atom during molecular dynamics. The initial temperature of the molecular dynamics search was 1000 K, and the search was continued until the self-adjusting temperature parameter exceeded 2000 K. (The minima hopping algorithm raises the search temperature as no new minima are found.)

3. Results and discussion

3.1. Synthesis

Fig. 1 shows schematics of the two-step synthesis of TMC/rGO nanocomposites, which we have previously reported on for the synthesis of molybdenum carbide/rGO nanocomposites [32]. Herein, we extend the method to the syntheses of tungsten carbide/rGO and iron carbide/rGO nanocomposites. In the first step—the solvothermal precipitation—the metal oxides (carbide precursors) were successfully deposited onto the rGO substrates, as shown in Fig. 2. Molybdenum oxide particles deposited on the rGO were well-dispersed (Fig. 2(a)) showing crystallite size of 31.1 nm, whereas those of iron oxide were formed as rod-like shape (Fig. 2(b)) with relatively large crystallite size of 74.5 nm. The Fe_3O_4 nanorods do not appear to be intimately attached to the carbon substrate, which as a result appears smooth. In the case of tungsten oxide, two different types of crystals, WO_2 and WO_3, were formed with crystallite sizes of 41.7 and 39.2 nm, respectively, showing a certain degree of agglomerations between particles (Fig. 2(c)).

The second step—the carburization of the metal oxides—required different conditions depending on the metal species. The SEM images and XRD patterns of TMC/rGO catalysts are shown in Fig. 3. As we previously reported [32], the carburization of MoO_2 into Mo_2C was successful at relatively low temperature (650 °C) in an H_2 atmosphere, without a gas-phase carbon source. In this case, the rGO substrate must be serving as the carbon source for the transformation. The Mo_2C nanoparticles were also well-dispersed on the rGO substrate showing smaller crystallite size (13.5 nm) compared to that of MoO_2. In the case of carburization of Fe_3O_4, temperatures above 750 °C in H_2 produced only large particle agglomerates without transformation, but adding an exogenous carbon source, CH_4, facilitated the transformation to Fe_3C. This may be attributable to the rod-like morphology of Fe_3O_4 particles, which do not intimately contact to the substrate and constrain the carbon transfer from rGO. Interestingly, those rod-like morphology of Fe_3O_4 changed dramatically during this process to nano-particulate Fe_3C. The crystallite sizes also decreased to a large extent from 74.5 (Fe_3O_4) to 23.3 nm (Fe_3C). A slight growth of carbon nano-fibers was observed around the particles, likely due to the use of additional CH_4. In the case of carburization of WO_2 and WO_3, neither the pure H_2 or CH_4/H_2 gas mixture led to the transformation into carbides, even above 1000 °C. However, a decrease in H_2 partial pressure—by using a 5% H_2/Ar gas mixture—and very slow ramp rate (1 °C/min) were successful in creating tungsten carbides. After this process, we also could obtain two different tungsten carbide crystals, WC and W_2C, supported on the rGO substrate. As shown in Fig. 3(c), tungsten carbide nanoparticles were still agglomerated to some extent, but their crystallite sizes ranged between 16.4 and 18.8 nm indicating that severe sintering and particle growth did not occur during the carburization process.

The proportion of nanoparticles' surface area that contacts the substrate should increase with decreasing size of nanoparticles. The crystallite sizes of all the carbide nanoparticulates were smaller than those of their parent oxides, suggesting that the contact between the

rGO substrate and the particles became more intimate due to the reconstruction of the particles during the carburization process.

3.2. Characterization and catalytic performance

In general, the electrocatalytic activity of a material is strongly affected by the accessibility of the reactant to the catalyst surface sites. If the carbide catalysts exhibited clear peaks for the underpotential deposition of hydrogen—such as is the case for Pt-based electrocatalysts [49]—we could directly integrate the peak area to evaluate the electrochemically active surface area. However, the carbide catalysts prepared in the present study showed no such peaks. Instead, as shown in Fig. S1, we used measurements of the electric double-layer capacitances (C_{dl}) to serve as an indicator of the active surface area; this is summarized in Table 2.

When the C_{dl} values were compared within the bulk carbides, WC showed higher C_{dl} than the other two bulk carbides, presumably because of its large surface area resulting from relatively small particle sizes (Mo_2C, Fe_3C, ~3 μm; WC, ~2 μm). The rGO-supported catalysts showed 5–8 times higher C_{dl} values than their bulk carbides. In this case, however, even though WC·W_2C/rGO exhibited agglomerations between particles to some extent and larger crystallite size than Mo_2C/rGO, the C_{dl} of WC·W_2C/rGO was twice as high than that of Mo_2C/rGO. These results suggest that the capacitance of the rGO-supported carbides catalysts were not only attributed to the size of carbide nanoparticles but also to other structural factors induced from the rGO substrate. In fact, the carbothermal process step can cause a partial exfoliation of the graphite oxide to create internal surface area. However, these two contributions to the capacitance are difficult to decouple.

Charge-transfer properties make up another essential characteristic of electrocatalyst systems. The Nyquist plots of the potentiostatic electrochemical impedance spectroscopy (PEIS) responses are shown in Fig. 4. For bulk carbide catalysts, the PEIS responses were successfully fit with a single-constant phase element (CPE) model comprised of a series resistance, R_s, a charge-transfer resistance, R_{ct}, and its corresponding CPE. The charge transfer process at the interface between the catalyst and electrolyte appeared as a semicircle in the Nyquist plot. The calculated R_{ct} value of bulk WC (69.5 Ω) was significantly lower than those of bulk Mo_2C (217.5 Ω) and bulk Fe_3C (445.7 Ω).

The Nyquist plots obtained using the rGO-supported carbide catalysts exhibited two semicircles, indicating that a different model is required to describe the responses. A two-CPE model, containing additional resistance related to the surface porosity, R_p, has been used for electrocatalysts having porous surface structures [50]. As shown in Fig. S1, the porous rGO substrate offered a large surface area and the two-CPE model was found to be capable of fitting their PEIS responses. Among the rGO-supported carbide catalysts, WC·W_2C/rGO exhibited the lowest R_{ct} (11.2 Ω), followed by Mo_2C/rGO (33.0 Ω) and Fe_3C/rGO (233.8 Ω). This tendency is the same as that of the bulk carbides (WC < Mo_2C < Fe_3C). The R_{ct} values of the rGO-supported carbide catalysts were reduced to a large extent compared to those of their bulk carbides, suggesting that high conductivity of the rGO substrate effectively enhanced the electron-transport process for the HER. The R_{ct} values obtained were also listed in Table 2.

Polarization curves of these catalysts are shown in Fig. 5(a) on the basis of the geometric current density. As is well known, Pt/C showed the highest activity for HER with nearly zero onset potential. For the carbide catalysts, it was difficult to define the onset potential due to their gradual increases in current densities. Instead, as suggested in previous studies [24,28,27], we compared the overpotential required for driving a certain current (-5 mA/cm^2 in the present study) as a practical metric for the HER activity, which are also listed as η_5 in Table 2. HER activities of the bulk carbide catalysts appeared to be well correlated to the electrocatalytic characteristics, such as surface area and conductivity, that is, a catalyst that exhibited lower R_{ct} and higher
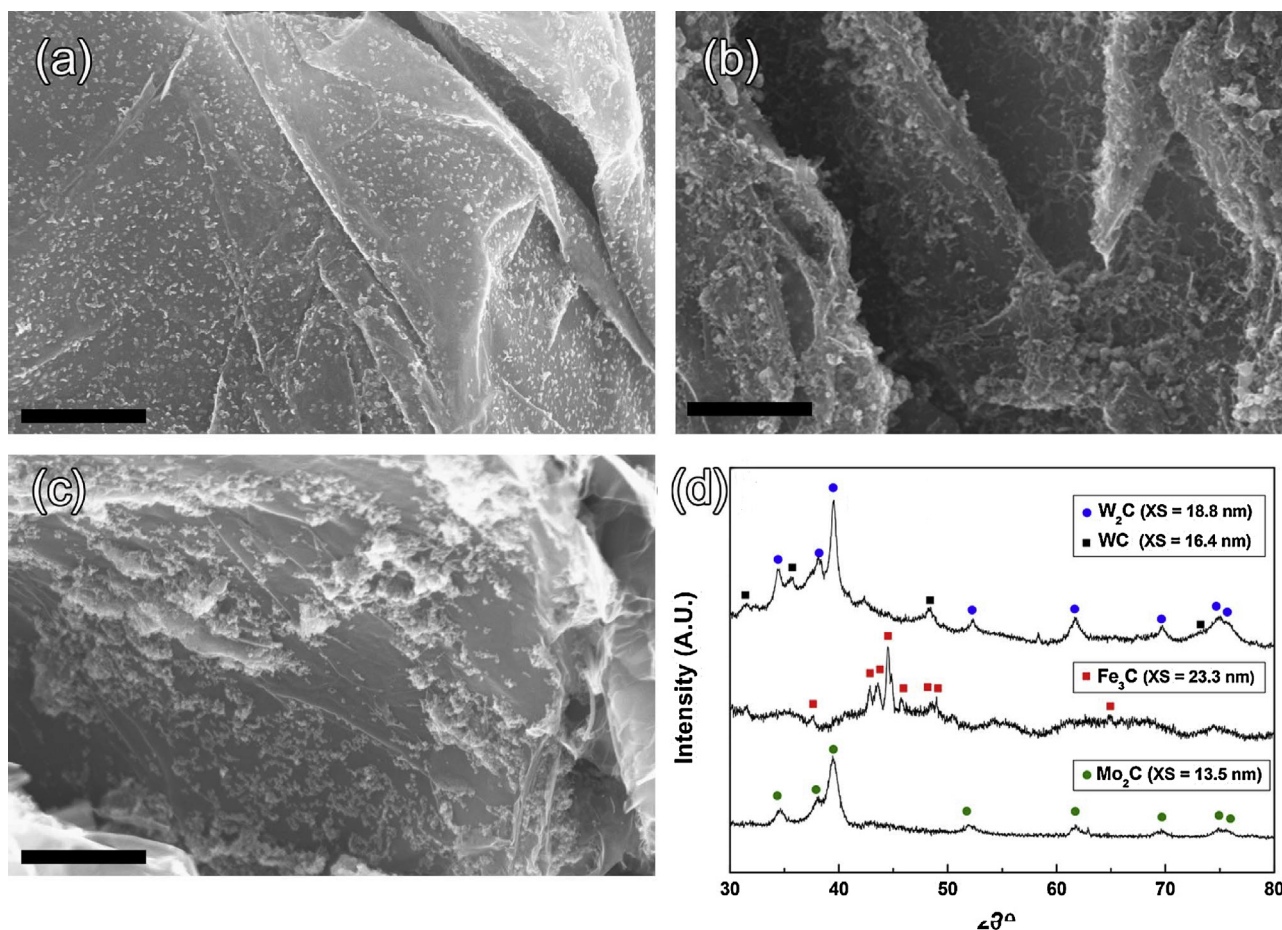
Fig. 3. Scanning electron microscopy (SEM) images of (a) Mo$_2$C/rGO, (b) Fe$_3$C/rGO, and (c) WC·W$_2$C/rGO. The scale indicates 1 μm. (d) shows XRD patterns of rGO-supported metal carbides. XRD peaks were assigned using ICDD card numbers 35-776, 51-939, 35-772, and 35-787 for W$_2$C, WC, Fe$_3$C, and Mo$_2$C, respectively. Crystallite sizes (XS) calculated based on XRD were also shown.

Table 2
Electric double-layer capacitances (C_{dl}), charge transfer resistances (R_{ct}), and potential required to drive geometric current density of $-5\,\text{mA/cm}^2$ (η_5) of carbide catalysts.

Catalyst	C_{dl} (mF)	R_{ct} (Ω)	η_5 (V$_{RHE}$)
Bulk Mo$_2$C	0.3	217.5	−0.56
Mo$_2$C/rGO	2.3	33.0	−0.28
Bulk Fe$_3$C	0.2	445.7	−0.59
Fe$_3$C/rGO	1.3	233.8	−0.54
Bulk WC	0.9	69.5	−0.47
WC·W$_2$C/rGO	4.7	11.2	−0.38

C_{dl} values required lower overpotential, in the order of bulk WC ($\eta_5 = -0.47\,\text{V}_{RHE}$), bulk Mo$_2$C ($\eta_5 = -0.56\,\text{V}_{RHE}$), and bulk Fe$_3$C ($\eta_5 = -0.59\,\text{V}_{RHE}$).

By using the rGO as a catalyst substrate, the HER activity of a carbide material was improved as expected by the increased surface area (high C_{dl}) and enhanced conductivity (low R_{ct}), but the extent was different for each carbide material. The promotion effect of the rGO substrate on the HER activity was most pronounced for the Mo$_2$C/rGO by 0.28 V$_{RHE}$ of η_5 from bulk Mo$_2$C, while those for the WC·W$_2$C/rGO and Fe$_3$C/rGO were improved by only 0.09 and 0.05 V$_{RHE}$ of η_5, respectively, relative to their bulk carbide materials. We note that even though the WC·W$_2$C/rGO exhibited the lowest R_{ct} and highest C_{dl}, its required overpotential ($\eta_5 = -0.38\,\text{V}_{RHE}$) was larger than that of Mo$_2$C/rGO ($\eta_5 = -0.28\,\text{V}_{RHE}$). To minimize the activity contribution from the surface area, we normalized the current density of a catalyst

by its C_{dl} as shown in Fig. 5(b)–(d), where the Mo$_2$C/rGO exhibited obviously higher C_{dl}-normalized activity than bulk Mo$_2$C, while the WC·W$_2$C/rGO and Fe$_3$C/rGO exhibited similar or even lower C_{dl}-normalized activities, respectively, relative to their bulk carbides. These results indicate that the HER activity of the rGO-supported carbide catalysts are not fully explained in terms of surface area or electrical conductivity.

3.3. Free energy of H adsorption

The binding strength of atomic hydrogen on a catalyst surface is considered to be a useful descriptor of HER activity, which is typically portrayed with HER volcano plots [6–8], which overall suggest that the closer the H binding free energy (ΔG_B[H]) is to the HER equilibrium (i.e., 0 eV relative to H$_2$ gas), the higher HER activity the catalyst exhibits. In a previous study [20], ΔG_B[H] for TMC and their HER activities were also reported to follow the general trend, but effects of surface structures on ΔG_B[H] were not directly examined, which would provide insights into particle size effects.

The nano-sized carbide particles dispersed on the rGO substrate are likely to have much smaller radii of curvature (that is, a larger fraction of edge sites on the surface) compared to the bulk carbides. To understand the reactivities of differing binding sites and terminations, as characterized by ΔG_B[H], surfaces of bulk and nano-sized carbides were modeled as flat and stepped structures using density functional theory calculations.

The hydrogen adsorption sites that exist on a surface unit cell were searched using the constrained minima-hopping algorithm (shown in
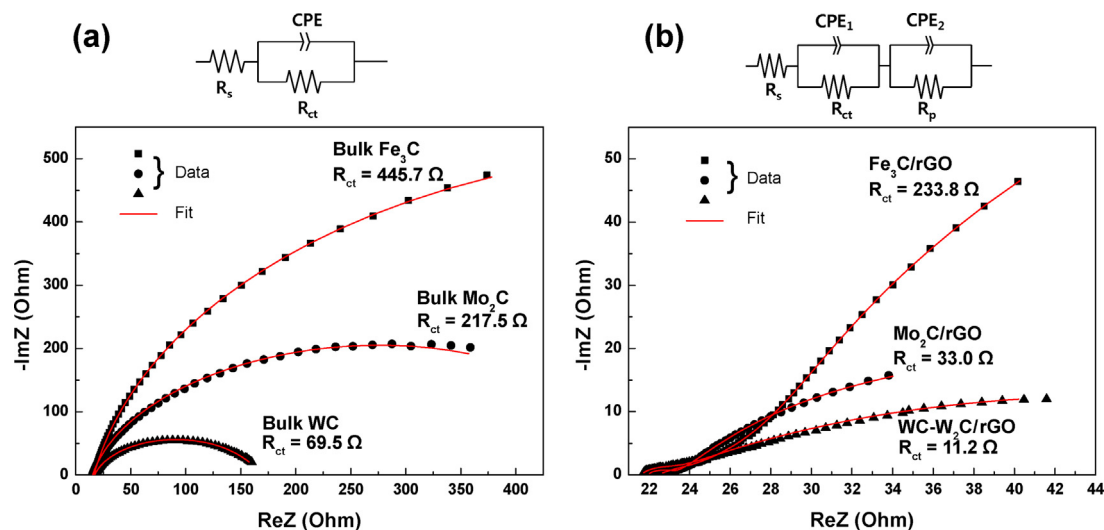
Fig. 4. Nyquist plots showing PEIS responses of (a) bulk carbides and (b) rGO-supported carbides at $-0.4\ V_{RHE}$. Equivalent circuit models for fitting the responses are shown at the top of plots.
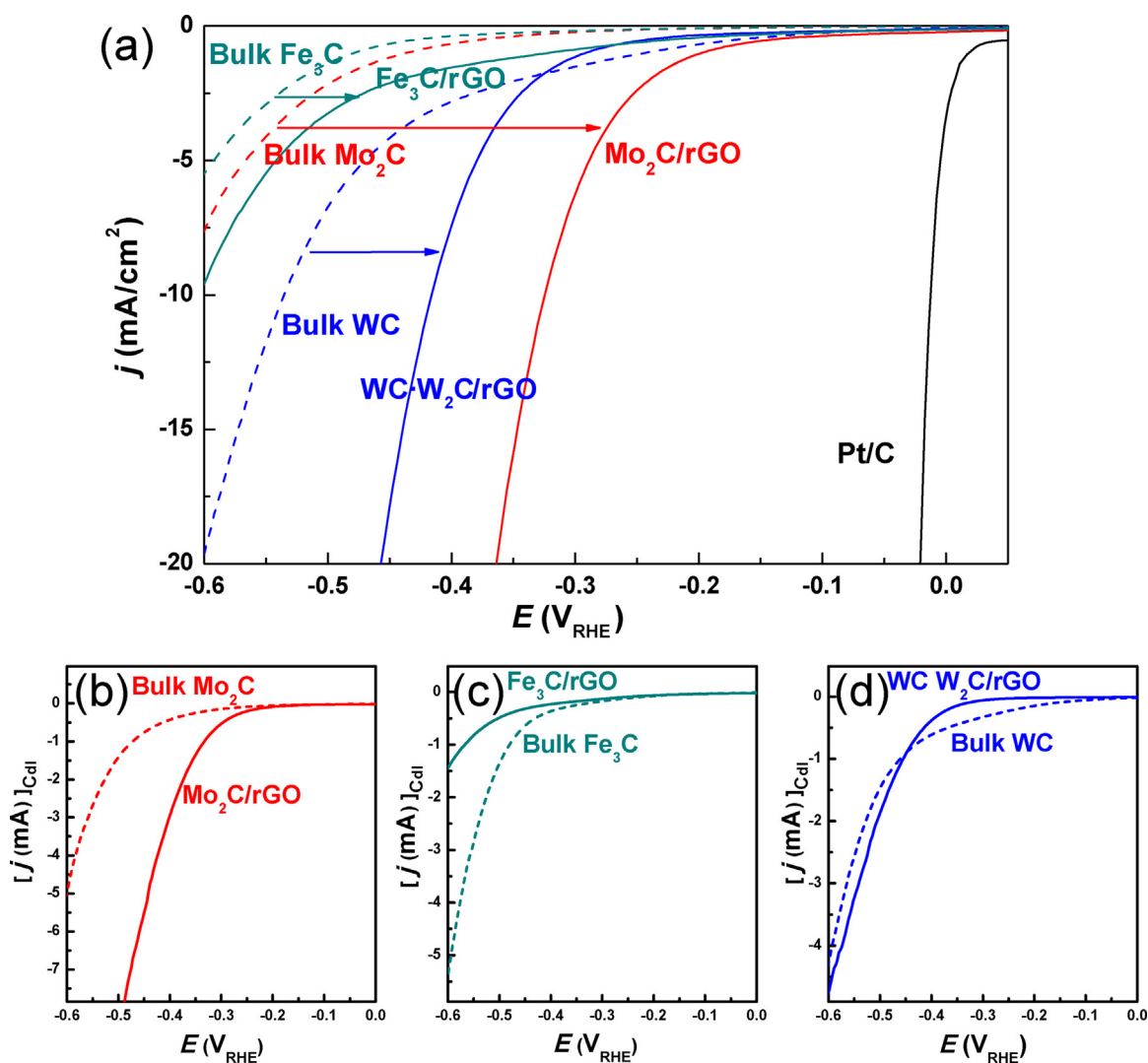

Fig. 5. (a) Polarization curves of Pt/C, bulk and rGO-supported carbide catalysts on the basis of geometric current density. (b–d) show comparisons between bulk Mo_2C and Mo_2C/rGO, bulk Fe_3C and Fe_3C/rGO, and bulk WC and WC·W_2C/rGO, respectively, on the basis of geometric current density normalized by corresponding double-layer capacitance. Bulk and rGO-supported carbide catalysts are shown with dashed and solid lines, respectively.
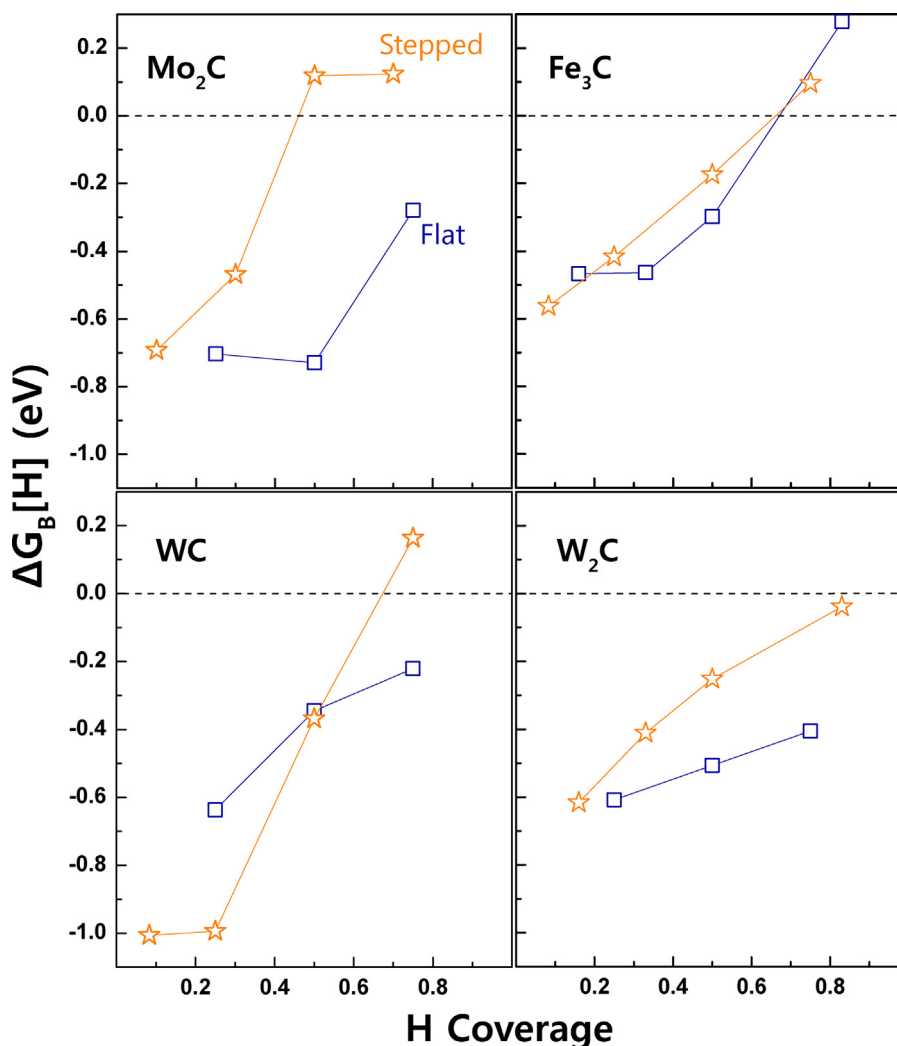
Fig. 6. Free energy of the H adsorption on the flat and stepped surfaces of Mo_2C, Fe_3C, WC, and W_2C with various H coverages ($0 < \theta < 1$). The weakest binding energies are reported for multiple H atoms adsorbed. Equilibrium for HER (0 eV) is shown as dashed line. $T = 298$ K, $P_{H_2} = 1$ bar. Surface structures and adsorption sites at each coverage are shown in detail in the Supporting Information.

Figs. S2–S5) [47]. On the flat surfaces, representing bulk powder carbides, only 3–5 different sites were present for hydrogen adsorption, and most of these sites exhibited highly exergonic $\Delta G_B[H]$ with narrow distributions. This suggests that the HER activities of the unsupported carbides are constrained by the desorption step that produces H_2. In contrast, a large number of hydrogen adsorption sites were found to be present on the stepped surfaces, resulting in much broader $\Delta G_B[H]$ distributions compared to the flat surfaces.

Free energies of hydrogen adsorption with various surface coverages are illustrated in Fig. 6. In the case of Mo_2C, the stepped surface appeared clearly advantageous on the thermodynamics of the HER over the range of hydrogen coverage explored in the present study, that is, the adsorption sites on the stepped surface exhibited the weaker $\Delta G_B[H]$'s than those on the flat surface, suggesting that the desorption process can be facilitated by making Mo_2C as a nanoparticle. For other carbides, however, it was difficult to assess that the stepped surface is advantageous to the HER thermodynamics. In the case of Fe_3C, the $\Delta G_B[H]$ on both surfaces behaved similarly with increasing with H coverage. The stepped surface of WC exhibited stronger adsorptions than the flat surface when the coverage was less than 0.5, indicating detrimental effects of the stepped surface on the HER thermodynamics at low coverages. On the contrary to this, the $\Delta G_B[H]$'s for the stepped surface of W_2C appeared to be closer to the equilibrium than those for the flat surface, which is similar to the behavior over Mo_2C.

Perhaps counter to intuition, both the experimental and theoretical results point to stepped surfaces having higher activity than flat surfaces for Mo_2C and W_2C. The carbides are considered to sit on the over-binding side of the hydrogen-evolution volcano [20], and since low-coordinated adsorption sites (such as edges, kinks, and corners) tend to bind adsorbates more strongly than high-coordinated sites [51], we should expect the stepped surfaces to be less active. Indeed, at the lowest hydrogen coverage, the general trend of stepped surfaces binding more strongly was validated by the computational results (see Fig. S6 in the Supporting Information for a complete summary of the energy of all configurations found via constrained minima hopping). However, as the H coverage increases, the stepped surfaces of Mo_2C, WC, and W_2C exhibited drastic decreases in H binding energy compared to their corresponding flat surfaces, while for Fe_3C both surfaces changed to a similar extent. As indicated from the broader $\Delta G_B[H]$ distributions, the stepped carbide surfaces are composed of various types of adsorption sites, including low-coordinated, high-coordinated, and exposed carbon sites. At higher H coverage, the low-coordinated adsorption sites that strongly bind H would be inactive by an occupation of H and only the weak-binding sites, such as groove and carbon sites, would be active for reaction. Indeed, some of these weak-binding sites—in particular the groove sites—exist only on the stepped surfaces of Mo_2C and W_2C, as can be seen in Figs. S2–S4 of the Supporting Information. This may help to explain how Mo_2C and W_2C show

improved per-site reactivity with stepped surfaces.

A second notable aspect of the stepped Mo_2C surface that arises from the binding-energy calculations is the region where the incremental binding energy crosses $\Delta G_B[H] = 0$ (the dashed line in Fig. 6); specifically, it exceeds the equilibrium free energy at a lower H coverage than the other materials and has a wider range of coverages where $\Delta G_B[H] \approx 0$. Given that hydrogen atoms adsorbed after this point more easily react off the surface as H_2, the stepped Mo_2C surface can be expected to show higher activity than the others over a wider range of H coverage. A more complete mechanistic analysis that includes barriers as a function of coverage and potential would be needed to make conclusive statements on the preferential surfaces, but these calculations generally support the notion that the stepped surface of Mo_2C is advantageous for HER.

3.4. Tafel analysis

To further our understanding of the experimental results, we conducted kinetic analyses on the HER mechanism, including analyses of the apparent rate-limiting steps and surface hydrogen coverages. Tafel plot analyses can provide useful insights into the HER mechanism. Especially, the Tafel slope, b, that is obtained by fitting the linear portion of the plot to the Tafel equation,

$$\eta = b \cdot \log j + a \qquad (3)$$

is reportedly [52] determined by the rate-limiting step of the HER. In the above equation, η is the cathodic overpotential and j is the current density. The HER mechanism in an acidic medium is generally described by either consecutive electrochemical reactions (Volmer–Heyrovsky):

$$2H^+ + 2e^- + * \xrightarrow{Volmer} H^* + H^+ + e^- \xrightarrow{Heyrovsky} H_2 + * \qquad (4)$$
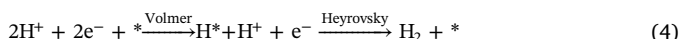
or by an initial electrochemical proton-deposition reaction combined with the surface reaction between two adsorbed hydrogen atoms (Volmer–Tafel):

$$2H^+ + 2e^- + 2* \xrightarrow{Volmer} 2H^* \xrightarrow{Tafel} H_2 + 2* \qquad (5)$$
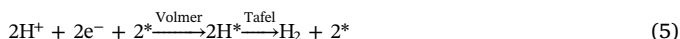
where * denotes an active site of the catalyst surface for the hydrogen adsorption.

Previous microkinetic analyses proposed diagnostic criteria that only three distinct Tafel slope values are available under the assumption of a negligible surface coverage of hydrogen ($\theta_H \sim 0$) that is potential-independent (steady-state) at an ambient temperature [52,53]. A Tafel slope of about $-40\,mV/dec$ suggests that the HER proceeds via the Volmer–Heyrovsky mechanism (4) and the Heyrovsky step is rate-limiting, while a Tafel slope of about $-30\,mV/dec$ suggests that it proceeds via the Volmer–Tafel mechanism (5) and the Tafel step is rate-

limiting. Finally, if the Volmer step is rate-limiting, the Tafel slope will be about $-120\,mV/dec$ regardless of the subsequent step.

However, as shown in Fig. 7(a), the Tafel slopes of the bulk carbide catalysts departed far from the "allowed" values, and their HER mechanisms could not be interpreted based on the above-mentioned classifications. One possible explanation for such steep Tafel slopes ($< -120\,mV/dec$) is a delay in the HER kinetics caused by the surface hydrogen that occupy more active sites as η increases [54,55]. This phenomenon is only explicable for the Volmer–Tafel mechanism (5) where the Tafel step is rate-limiting [54,55]. For an extreme example, if θ_H gets close to 1 at large η, the Tafel slope value will be infinite ($b = -\infty$) showing a limiting current. If the HER rate is limited by either the Volmer or Heyrovsky step and the high θ_H is taken into account, the Tafel slope value will be $-120\,mV/dec$. [54,55] Thus, the Tafel slope values of the bulk carbide catalysts in the present study suggest that the overall HER rate is limited by the Tafel step and that a certain fraction of the active sites are blocked by strongly-bound surface H atoms. We note that the quantification of θ_H is not straightforward because it depends on η, but it appeared not to fully occupy all the active sites ($b \neq -\infty$) at the region of η applied in the present study (up to $-0.6\,V_{RHE}$).

The rGO-supported carbide catalysts also exhibited steeper Tafel slopes than $-120\,mV/dec$ (Fig. 7(b)) also suggesting that the Tafel step is limiting the HER rate in the presence of surface H atoms. Even though the precise quantification of θ_H was not feasible, the Tafel slope values allowed us to compare the relative θ_H in a qualitative manner. In the cases of the Mo_2C/rGO and $WC\cdot W_2C/rGO$, their θ_H are expected to be lower than those of their bulk carbide catalysts based on the less steep Tafel slopes. In contrast, the much steeper Tafel slope of the Fe_3C/rGO than that of the bulk Fe_3C suggests higher θ_H on the surface of the Fe_3C/rGO.

These analyses on the HER mechanism can provide an explanation for the indirect correlation between the HER activity and the charge transfer resistance as shown above. Since the HER rates on these carbide catalysts appear limited by the non-electrochemical reaction (Tafel step), the enhanced charge transfer property does not necessarily promote the HER kinetics. Instead, as in the case of Mo_2C, the weakened hydrogen binding energy and the consequential decrease in θ_H by making the carbide to the nanoparticulates appeared to be more effective to accelerate the HER activity.

It is noteworthy that although numerous types of Mo_2C catalysts were synthesized and suggested as efficient cathodic materials for HER previously [31], the proposed mechanism for the reactions taking place on Mo_2C has not reached agreement. This may due to the fact that Tafel slope values observed in each report are distributed over a wide range, from -264 to $-28.9\,mV/dec$. [31] Based on our suggested HER mechanism—that the hydrogen coverage determines the overall kinetics—the variation of the reported values can be explained by different extents of θ_H which is largely dependent on the surface structure, pH, temperature, and so on.
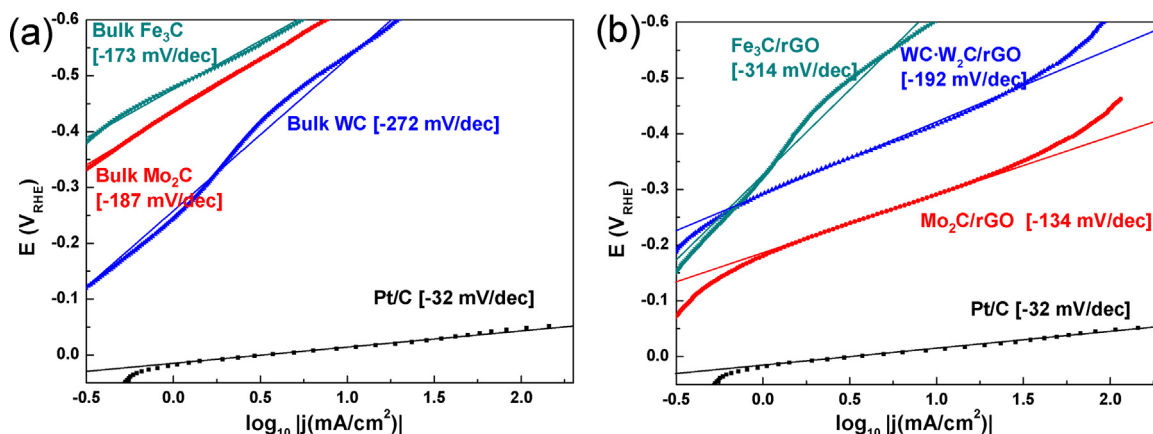

Fig. 7. Tafel plots of (a) bulk and (b) rGO-supported carbide catalysts in comparison with Pt/C. Tafel slope values were shown in both figures.

In the case of the simpler Pt structure, however, its θ_H and resulting HER performance appears less sensitive to such factors. In agreement with previous studies [56–58], Pt/C exhibited a Tafel slope of $-32\,mV/$ dec. The previous studies suggest a typical Volmer–Tafel mechanism where the Tafel step is rate-limiting without surface H that binds strongly and hinders the HER. Based on the observation that the total amount of adsorbed H was more than 1 monolayer relative to the number of surface Pt atoms [59], the Pt surface had been considered to be fully covered by H during the HER. However, later spectroscopic studies revealed that the H atoms are likely to be absorbed underneath the surface layer (subsurface) so that the active site of the Pt surface remained unoccupied, [60,61] exhibiting more complexity in the simpler Pt system as well.

4. Conclusion

Three types of TMC nanoparticles, Mo_2C, Fe_3C, and $WC\cdot W_2C$, dispersed on the rGO substrate (TMC/rGO) were prepared by a two-step synthesis (solvothermal + carburization) and their catalytic activities for the HER were compared to those of bulk TMC powders in consideration of two major effects: the charge transfer and particle size.

Potentiostatic impedance spectroscopy showed that the charge transfer resistance (R_{ct}) of each TMC/rGO catalyst was drastically reduced compared to that of bulk TMC catalyst, suggesting higher electronic conductivity could be obtained by using rGO as the substrate of the electrocatalyst. However, the correlation between R_{ct} and the HER activity appeared not to be strong. Among the TMCs, only Mo_2C/rGO obviously exhibited higher intrinsic activity than bulk Mo_2C.

The particle size effects of the TMCs were investigated by DFT calculations, in which the free energies of the atomic hydrogen adsorption ($\Delta G_B[H]$) on the flat and stepped surfaces were compared. For all the TMC surfaces, $\Delta G_B[H]$'s were calculated to be highly exergonic, indicating that weakening the adsorption strength could facilitate the desorption step forming H_2 and result in the increase in the HER activity. The hydrogen bindings on the stepped Mo_2C surface were weaker than those on the flat Mo_2C surface, which serve as an explanation of Mo_2C nanoparticles' higher activity than bulk Mo_2C. In contrast, no clear tendencies were found between the flat and stepped surfaces of the other TMCs (Fe_3C, WC and W_2C).

Tafel analyses allowed for the distinction of the rate-limiting step of HER on the TMC catalysts. Based on the Tafel slope values steeper than $-120\,mV/dec$, recombination reaction between surface hydrogen atoms (Tafel step) was considered as the rate-limiting step, which provide an explain for the indirect effect of the charge transfer property on the HER activity of the TMC catalysts.

Appendix A. Supplementary data

Supplementary data associated with this article can be found, in the online version, at https://doi.org/10.1016/j.apcatb.2018.04.032.

References

[1] J.O. Bockris, Int. J. Hydrogen Energy 27 (2002) 731–740.
[2] N. Armaroli, V. Balzani, ChemSusChem 4 (2011) 21–36.
[3] C. Acar, I. Dincer, Int. J. Hydrogen Energy 39 (2014) 1–12.
[4] P.C.K. Vesborg, B. Seger, I. Chorkendorff, J. Phys. Chem. Lett. 6 (2015) 951–957.
[5] M.G. Walter, E.L. Warren, J.R. McKone, S.W. Boettcher, Q. Mi, E.A. Santori, N.S. Lewis, Chem. Rev. 110 (2010) 6446–6473.
[6] S. Trasatti, J. Electroanal. Chem. Interfacial Electrochem. 39 (1972) 163–184.
[7] J.K. Nørskov, T. Bligaard, A. Logadottir, J.R. Kitchin, J.G. Chen, S. Pandelov, U. Stimming, J. Electrochem. Soc. 152 (2005) J23–J26.
[8] J. Greeley, T.F. Jaramillo, J. Bonde, I. Chorkendorff, J.K. Nørskov, Nat. Mater. 5 (2006) 909–913.
[9] D. Voiry, M. Salehi, R. Silva, T. Fujita, M. Chen, T. Asefa, V.B. Shenoy, G. Eda, M. Chhowalla, Nano Lett. 13 (2013) 6222–6227.
[10] D.R. Cummins, U. Martinez, A. Sherehiy, R. Kappera, A. Martinez-Garcia, R.K. Schulze, J. Jasinski, J. Zhang, R.K. Gupta, J. Lou, M. Chhowalla, G. Sumanasekera, A.D. Mohite, M.K. Sunkara, G. Gupta, Nat. Commun. 7 (2016) 11857.
[11] G. Tsirlina, O. Petrii, Electrochim. Acta 32 (1987) 649–657.
[12] H. Zheng, J. Huang, W. Wang, C. Ma, Electrochem. Commun. 7 (2005) 1045–1049.
[13] D.J. Ham, R. Ganesan, J.S. Lee, Int. J. Hydrogen Energy 33 (2008) 6865–6872.
[14] T. Ferri, D. Gozzi, A. Latini, Int. J. Hydrogen Energy 32 (2007) 4692–4701.
[15] Y.C. Kimmel, D.V. Esposito, R.W. Birkmire, J.G. Chen, Int. J. Hydrogen Energy 37 (2012) 3019–3024.
[16] D.V. Esposito, S.T. Hunt, Y.C. Kimmel, J.G. Chen, J. Am. Chem. Soc. 134 (2012) 3025–3033.
[17] S. Wirth, F. Harnisch, M. Weinmann, U. Schröder, Appl. Catal. B 126 (2012) 225–230.
[18] W.-F. Chen, J.T. Muckerman, E. Fujita, Chem. Commun. 49 (2013) 8896–8909.
[19] Y. Yan, B. Xia, X. Qi, H. Wang, R. Xu, J.-Y. Wang, H. Zhang, X. Wang, Chem. Commun. 49 (2013) 4884–4886.
[20] R. Michalsky, Y.-J. Zhang, A.A. Peterson, ACS Catal. 4 (2014) 1274–1278.
[21] R. Michalsky, Y.-J. Zhang, A.J. Medford, A.A. Peterson, J. Phys. Chem. C 118 (2014) 13026–13034.
[22] L. Liao, S. Wang, J. Xiao, X. Bian, Y. Zhang, M.D. Scanlon, X. Hu, Y. Tang, B. Liu, H.H. Girault, Energy Environ. Sci. 7 (2014) 387–392.
[23] H.B. Wu, B.Y. Xia, L. Yu, X.-Y. Yu, X.W.D. Lou, Nat. Commun. 6 (2015).
[24] W.-F. Chen, C.-H. Wang, K. Sasaki, N. Marinkovic, W. Xu, J.T. Muckerman, Y. Zhu, R.R. Adzic, Energy Environ. Sci. 6 (2013) 943–951.
[25] N.S. Alhajri, D.H. Anjum, K. Takanabe, J. Mater. Chem. A 2 (2014) 10548–10556.
[26] L.F. Pan, Y.H. Li, S. Yang, P.F. Liu, M.Q. Yu, H.G. Yang, Chem. Commun. 50 (2014) 13135–13137.
[27] D.H. Youn, S. Han, J.Y. Kim, J.Y. Kim, H. Park, S.H. Choi, J.S. Lee, ACS Nano 8 (2014) 5164–5173.
[28] S.T. Hunt, T. Nimmanwudipong, Y. Román-Leshkov, Angew. Chem. Int. Ed. 53 (2014) 5131–5136.
[29] J. Wang, G. Wang, S. Miao, J. Li, X. Bao, Faraday Discuss. 176 (2014) 135–151.
[30] J.-S. Li, Y. Wang, C.-H. Liu, S.-L. Li, Y.-G. Wang, L.-Z. Dong, Z.-H. Dai, Y.-F. Li, Y.-Q. Lan, Nat. Commun. 7 (2016) 11204.
[31] M. Miao, J. Pan, T. He, Y. Yan, B.Y. Xia, X. Wang, Chem. Eur. J. 23 (2017) 10947–10961.
[32] S.K. Kim, D. Yoon, S.-C. Lee, J. Kim, ACS Catal. 5 (2015) 3292–3303.
[33] W.S. Hummers, R.E. Offeman, J. Am. Chem. Soc. 80 (1958) 1339–1339.
[34] N.I. Kovtyukhova, P.J. Ollivier, B.R. Martin, T.E. Mallouk, S.A. Chizhik, E.V. Buzaneva, A.D. Gorchinskiy, Chem. Mater. 11 (1999) 771–778.
[35] T.Y. Kosolapova, Carbides: Properties, Production, and Applications, Plenum Press, New York, 1971, pp. 75–182.
[36] R. Chen, C. Yang, W. Cai, H.-Y. Wang, J. Miao, L. Zhang, S. Chen, B. Liu, ACS Energy Lett. 2 (2017) 1070–1075.
[37] R. Wei, M. Fang, G. Dong, J.C. Ho, Sci. Bull. 62 (2017) 971–973.
[38] Y.C. Kimmel, X. Xu, W. Yu, X. Yang, J.G. Chen, ACS Catal. 4 (2014) 1558–1562.
[39] K.P. Kuhl, E.R. Cave, D.N. Abram, T.F. Jaramillo, Energy Environ. Sci. 5 (2012) 7050–7059.
[40] A.J. Bard, L.R. Faulkner, Electrochemical Methods: Fundamentals and Applications, 2nd ed., Wiley, New York, 2001, pp. 226–260.
[41] D. Vanderbilt, Phys. Rev. B 41 (1990) 7892–7895.
[42] S.R. Bahn, K.W. Jacobsen, Comput. Sci. Eng. 4 (2002) 56–66.
[43] B. Hammer, L.B. Hansen, J.K. Nørskov, Phys. Rev. B 59 (1999) 7413–7421.
[44] T. Epicier, J. Dubois, C. Esnouf, G. Fantozzi, P. Convert, Acta Metall. 36 (1988) 1903–1921.
[45] I.G. Wood, L. Vočadlo, K.S. Knight, D.P. Dobson, W.G. Marshall, G.D. Price, J. Brodholt, J. Appl. Crystallogr. 37 (2004) 82–90.
[46] K. Page, J. Li, R. Savinelli, H.N. Szumila, J. Zhang, J.K. Stalick, T. Proffen, S.L. Scott, R. Seshadri, Solid State Sci. 10 (2008) 1499–1510.
[47] A.A. Peterson, Top. Catal. 57 (2014) 40–53.
[48] S. Goedecker, J. Chem. Phys. 120 (2004) 9911–9917.
[49] B. Lim, M. Jiang, P.H.C. Camargo, E.C. Cho, J. Tao, X. Lu, Y. Zhu, Y. Xia, Science 324 (2009) 1302–1305.
[50] B. Łosiewicz, A. Budniok, E. Rówiński, E. Łągiewka, A. Lasia, Int. J. Hydrogen Energy 29 (2004) 145–157.
[51] A.A. Peterson, L.C. Grabow, T.P. Brennan, B. Shong, C. Ooi, D.M. Wu, C.W. Li, A. Kushwaha, A.J. Medford, F. Mbuga, L. Li, J.K. Nørskov, Top. Catal. 55 (2012) 1276–1282.
[52] J.O. Bockris, E.C. Potter, J. Electrochem. Soc. 99 (1952) 169–186.
[53] B.E. Conway, B.V. Tilak, D.D. Eley, P.W.H. Pines (Eds.), Advance in Catalysis, vol. 38, Academic Press Inc, New York, 1992, pp. 1–147.
[54] M.R.G. de Chialvo, A.C. Chialvo, Electrochim. Acta 44 (1998) 841–851.
[55] B.E. Conway, B.V. Tilak, Electrochim. Acta 47 (2002) 3571–3594.
[56] H. Kita, J. Res. Inst. Catal. Hokkaido Univ. 13 (1965) 151–168.
[57] B.E. Conway, J.O. Bockris, J. Chem. Phys. 26 (1957) 532–541.
[58] O.A. Petrii, G.A. Tsirlina, Electrochim. Acta 39 (1994) 1739–1747.
[59] B.E. Conway, L. Bai, J. Electroanal. Chem. Interfacial Electrochem. 198 (1986) 149–175.
[60] I.M. Tidswell, N.M. Marković, P.N. Ross, J. Electroanal. Chem. 376 (1994) 119–126.
[61] C.A. Lucas, N.M. Marković, P.N. Ross, Phys. Rev. Lett. 77 (1996) 4922–4925.